Retrieval of Ocean Surface Wave Parameters from ICESat-2 Altimetry: Validation and Limitations

Lang Cao,[a] Qingxiang Liu,[a,b], Joey Voermans[b], Alberto Alberello[c], Alexander Babanin[b]

[a] *State Key Laboratory of Physical Oceanography, Ocean University of China*

[b] *Department of Infrastructure Engineering, University of Melbourne, Melbourne, Australia*

[c]*School of Engineering, Mathematics and Physics, University of East Anglia, Norwich, UK*

Corresponding author: Qingxiang Liu, liuqingxiang@ouc.edu.cn

ABSTRACT

The Ice, Cloud, and land Elevation Satellite 2 (ICESat-2) provides high-resolution height measurements of the Earth's ice, land and ocean surfaces, making it possible to observe individual waves in the global ocean. Here, we use approximately 3-yr ICESat-2 laser altimetry data (October 2018 to August 2021), from which ocean surface wave parameters, including significant wave height, peak wave length and direction, are retrieved and thoroughly validated against in situ observations in both open ocean and coastal waters. It is found that the ICESat-2 wave height agrees very well with buoy measurements, featuring a RMSE of 0.16 (0.26) m in deep (coastal) waters. The peak wave length and direction from ICESat-2, though less favorable, remain practically useful, showing a correlation coefficient of about 0.7 with buoy data. The challenge in estimating peak wave length and direction from ICESat-2 along-track surface profiles under mixed sea states are discussed through numerical simulations and buoy observations.

Keywords: ocean surface waves, ICESat-2, significant wave height, peak wave length, peak wave direction, mixed sea states

1. Introduction

Ocean surface waves are small-scale gravity waves generated by the interaction of wind and sea surface, and play an important role in ocean dynamical processes. The significant wave height and peak period of ocean surface waves are fundamental parameters used to describe the sea state (Piscopo et al. 2022), and are also key variables for explaining extreme sea level in coastal regions (Dodet et al. 2018). Obtaining accurate, stable and long-term wave parameters is thus crucial for extreme weather forecasting, coastal engineering design and wave climate studies (e.g., Ardhuin et al. 2019).

Wave parameters are currently available from in-situ buoys, spectral wave models, and satellite remote sensing. Surface buoys provide the most accurate in-situ wave measurements, but the majority of existing moored buoys are deployed in the coastal waters of North America and Western Europe, with large data gaps in the Southern Ocean and the tropics (e.g., Ardhuin et al. 2019). In addition, point source measurements of surface buoys do not accurately reflect the spatial pattern of the wave field. Third-generation spectral wave models, such as WAM (The WAMDI Group, 1988), WAVEWATCH III (Tolman et al. 2002) and SWAN (Booij et

al. 1999), have been used to forecast and hindcast the evolution of waves at global and regional scales (e.g., Chawla et al. 2013; Rogers et al. 2014; Liu et al. 2021), but may contain large errors in the Southern Ocean under strong wind forcing conditions (Aouf et al. 2021). Since the launch of GEOSAT in 1985, ocean satellites have been providing continuous global measurements of important wave properties such as the significant wave height (Ribal and Young 2019; Liu et al. 2023) and the directional spectrum (Shao et al. 2017; Hauser et al. 2021). In general radar altimetry estimates the significant wave height from the slope of the leading edge of the return signal (Young 1999), with a footprint diameter of 1–10 km (Chelton et al. 2001). However, the applicability of altimetry data in the coastal regions is limited by the size of the footprint which can be contaminated by non-Gaussian surfaces such as land and calm waters (Passaro et al. 2014).

The Ice, Cloud, and land Elevation Satellite 2 (ICESat-2), launched on 15 September 2018, measures the elevation of the Earth's ice, land, and ocean surfaces at high spatial resolution with its sole instrument, the Advanced Topographic Laser Altimeter System (ATLAS). The main objectives of ICESat-2 are to monitor changes in the heights of ice sheets and glaciers, as well as sea ice thickness distribution, in order to record the effects of a changing climate (Markus et al. 2017). The ATLAS instrument is a photon counting LiDAR that transmits green laser pulses (532 nm) at a rate of 10 kHz. It employs three pairs of laser beams to collect elevation data at 0.7 m intervals along ground tracks, with an average laser footprint diameter of 11 m (Magruder et al. 2021). Each beam pair consists of a strong beam and a weak beam with an energy ratio of approximately 4:1, and these two beams are separated by 90 m in the cross-track direction. The beam pairs are separated by about 3.3 km in the cross-track direction, and the strong and weak beams are separated by about 2.5 km in the along-track direction (Neumann et al. 2019). ICESat-2 laser altimetry data have centimeter-level accuracy, with the height accuracy better than $\pm$7.2 cm on flat reflective surfaces, such as the interior of the Antarctic ice sheet (Brunt et al. 2021), and the mean geolocation accuracy of about 3.5 m (Magruder et al. 2021). Due to the low reflectivity of ocean water, ATLAS generally detects 1 to 3 signal photons per laser shot in strong beams and 0.25 to 1 in weak beams (Neumann et al. 2022).

Klotz et al. (2020) first demonstrated that ICESat-2 was capable of observing individual waves and sea states in the ocean using a 4-month dataset. Yu et al. (2021) evaluated the ability of ICESat-2 ocean data to recover oceanographic signals, including ocean surface waves, in

the tropical Pacific (1.5-yr data). Nilsson et al. (2022) compared 1-yr ICESat-2 wave heights with coincident CryoSat-2 radar altimeter observations, and found high correlations between the two (1-yr data). Dietrich et al. (2023) further checked the ability of ICESat-2 to monitor coastal waves with less than 1-month data. Interestingly, the ICESat-2 wave data have also been used to derive water depth in opaque waters using the linear dispersion relationship of ocean waves (Yang et al. 2022). Several studies also showed that ICESat-2 measurements could be used to derive waves in the ice (Collard et al. 2022), wave-affected marginal ice zone width (Brouwer et al. 2022; Horvat et al. 2020) and ice-induced wave decay rates (Voermans et al. 2024).

Previous studies on the assessment of the ICESat-2 wave parameters generally considered data with fairly short duration or within limited geographical extents (e.g., Klotz et al. 2020; Yu et al. 2021; Dietrich et al. 2023). To thoroughly investigate the accuracy of ICESat-2 wave measurements, we fetch approximately 3-yr ICESat-2 laser altimetry data over the period from October 2018 to August 2021, from which wave parameters, including significant wave height H_s, peak wavelength L_p and peak wave direction θ_p, are derived and then compared against in-situ buoy observations in both deep ocean and coastal waters based on more than 80 buoy stations. The remaining sections are organized as follows. Section 2 presents a brief description of the ICESat-2 data, the theory and verification of along-track sampling, and the retrieval and validation methods of wave parameters. Section 3 presents the validation results of wave parameters in open oceans and coastal waters. We discuss the impact of multimodal sea states on the retrieval of ICESat-2 wave parameters in Section 4, along with the comparison against spectral wave models. A brief conclusion in Section 5 finalizes this paper.

2. Data and Methods

a. ICESat-2 data

The ICESat-2 mission's Level 2 data product, ATL03, is available through the National Snow and Ice Data Center (NSIDC), and, specifically, version 6 is used in this study (Neumann et al. 2023). The ATL03 global geolocated photon data provide precise latitude, longitude, elevation, and time for each received photon above the WGS84 ellipsoid. The data set spans from October 2018 to the present date, with a temporal resolution determined by the ICESat-2 repeat period (91 days). The along-track resolution of the ATL03 data can reach as high as 0.7 m under clear sky conditions (Neumann et al. 2022). The ATL03 data product provides a

surface type classification and a confidence assessment for each photon event. The confidence parameter enables signal and background photon events to be distinguished on five surface types, including land ice, sea ice, ocean, land and inland water. In order to generate a best estimate of the photon height, ATL03 applies geophysical corrections to account for the effect of atmosphere and solid earth deformation, and provides geophysical corrections as reference values (e.g., geoid, ocean tides, and dynamic atmospheric correction (Neumann et al. 2019)).

b. Along-track sampling: theory and verification

The high-resolution one-dimensional (1D) sampling of ocean surface height along the ground tracks enables the ICESat-2 to measure ocean surface waves. However, the measured wavelength is typically not the actual wavelength since ICESat-2 along-track measurements are generally not aligned with the direction of wave propagation. The misalignment between the two (i.e., the dominant wave direction and the track orientation) results in an overestimation of the wavelength by approximately a factor of $1/\cos\alpha$, where α is the angle between the wave direction and the track. The theoretical formulation of Yu et al. (2021) demonstrates the "distorting" effect of the along-tracking sampling nicely and, thus, is followed here.

For a unidirectional, monochromatic wave field η travelling along the x direction with a wavenumber k, radian frequency ω, amplitude a and initial phase φ_0, we have

$$\eta(x,t) = a\cos(kx - \omega t + \varphi_0)\,, \tag{1}$$

where $\omega^2 = \mathrm{g}k$ according to the deep-water dispersion relation is assumed, and g is the gravity acceleration. For a sensor flying over the wave field along the direction α relative to the x axis, the sea surface it samples is given by

$$\eta(r,t) = a\cos(kr\cos\alpha - \omega r/v_r + \varphi_0) = a\cos[(k\cos\alpha - \omega/v_r)r + \varphi_0]\,, \tag{2}$$

where r denotes the along-track distance and v_r is the ground orbital velocity of the sensor. Thus the apparent wavenumber k_a detected by the satellite sensor is

$$k_a = k(\cos\alpha - c/v_r), \tag{3}$$

and the apparent wavelength L_a reads

$$L_a = L/(\cos\alpha - c/v_r). \tag{4}$$

Here, $c = \omega/k$ is the wave phase velocity and $L = 2\pi/k$. For deep-water ocean surface waves with periods less than 30 s, $c \leq 46$ m s^{-1}, and for ICESat-2 ($v_r = 7$ km s^{-1}), $c/v_r \leq 0.01$. Hence we have $L_a \approx L/\cos\alpha$. Note that this also holds for coastal waters since c reduces as

water depth decreases. It is further noted that according to Eq. (2), the wave amplitude a is still well detected by the along-track sampling.

The formulation above assumes a simple, monochromatic wave field. It may be worthwhile to check whether Eq. (4) is applicable to irregular, directional sea states which are ubiquitous in real oceans. In doing so, we use the Wave Analysis for Fatigue and Oceanography (WAFO) MATLAB toolbox (Brodtkorb et al. 2000) to simulate "realistic" two-dimensional (2D), time-varying wave fields $\eta(x, y, t)$ for a given directional wave spectrum $E(f, \theta)$. In this paper, the wind sea spectral form of Donelan et al. (1985) is adopted:

$$E(f, \theta) = E(f)D(f, \theta), \tag{5}$$

$$E(f) = \beta \mathrm{g}^2 (2\pi)^{-4} f_p^{-1} f^{-4} \exp\left[-\left(\frac{f}{f_p}\right)^{-4}\right] \cdot \gamma_d^{\exp\left[\frac{-(f-f_p)^2}{2\sigma^2 f_p^2}\right]}, \tag{6}$$

$$\beta = 0.0165\nu^{0.55}, \tag{7}$$

$$\gamma_d = \begin{cases} 6.489 + 6\log\nu, & \nu \geq 0.159 \\ 1.7, & \nu < 0.159 \end{cases} \tag{8}$$

$$\sigma = 0.08 + 1.29 \times 10^{-3}\nu^{-3}, \tag{9}$$

where $E(f)$ is the frequency spectrum, f_p is the peak frequency, β is the high-frequency energy level, γ_d is the peak enhancement factor, σ is the peak width parameter, and ν represents the non-dimensional peak frequency $\nu = f_p U_{10}/\mathrm{g}$, in which U_{10} is the wind speed 10 m above the sea surface. The directional spreading function $D(f, \theta)$ reads

$$D(f, \theta) = 0.5\beta_s \mathrm{sech}^2 \beta\left[\theta - \theta_p(f)\right], \tag{10}$$

$$\beta_s = \begin{cases} 2.61\left(\frac{f}{f_p}\right)^{1.3}, & 0.56 < f/f_p < 0.95 \\ 2.28\left(\frac{f}{f_p}\right)^{-1.3}, & 0.95 < f/f_p < 1.6 \\ 10^{\left\{-0.4+0.8393\exp\left[-0.567\ln\left(\left(\frac{f}{f_p}\right)^2\right)\right]\right\}}, & f/f_p > 1.6 \end{cases} \tag{11}$$

where θ_p is the dominant wave direction at the given frequency f (Donelan et al. 1985; Banner 1990). For a given $E(f, \theta)$, the sea state $\eta(x, y, t)$ can be essentially reconstructed as

$$\eta(x, y, t) = \sum_i \sum_j a_{i,j} \cos\left[k_i\left(x\cos\theta_j + y\sin\theta_j\right) - \omega_i t + \varphi_{i,j}\right], \tag{12}$$

157 in which the amplitude $a_{i,j}$ could be estimated as

158 $$a_{i,j} = [2E(f,\theta)\Delta f \Delta\theta]^{1/2}, \quad (13)$$

159 and the initial phase $\varphi_{i,j}$ is assumed to be uniformly distributed.

160 Figure 1 illustrates the distorting effect of the ICESat-2 along-track sampling on the wave
161 spectrum and the corresponding peak wavelength for directional sea states. Here we use a
162 constant wind speed U_{10} of 15 m s^{-1} and the peak frequency f_p of 0.1 Hz, yielding the
163 frequency spectrum $E(f)$ shown in Fig. 1a with the wave height H_s of 5 m according to Eqs.
164 (6-9). The directional spectrum $E(f,\theta)$ shown in Fig. 1b, as an example, features a wind sea
165 system primarily coming from the east (the peak wave direction $\theta_p = 90°$), and almost
166 perpendicular to the ICESat-2 ground track (solid green line with the direction of 358°). A
167 zoomed-in view (i.e., 3 km × 2 km domain) of the wave field $\eta(x,y)$ on a 25 km × 25 km grid
168 ($\Delta x = \Delta y = 5$ m) corresponding to this $E(f,\theta)$ at a specific instant, as produced by the
169 WAFO toolbox, is demonstrated in Fig. 1c. We then can extract pseudo 1D surface profiles
170 from the prescribed wave field $\eta(x,y,t)$ by using the trajectory setting of the ICESat-2 three
171 strong beams (i.e., gt1r, gt2r, gt3r of the ICESat-2 strong beams; as an illustration, the gt2r
172 track is given in Fig. 1c as the green solid line). With these pseudo surface profiles, wave
173 parameters, including wave height H_s, apparent peak wavelength $L_{p,a}$ and wavenumber
174 spectrum $F(k)$ can be estimated using the methodology detailed in Section 2.c. The
175 comparisons between the estimated wave parameters and the true values, as a function of α
176 (the angle between θ_p and the track orientation) are presented in Figs. 1 (d-f). For statistical
177 reliability, 20 realizations of the random sea surface $\eta(x,y,t)$ for the given $E(f,\theta)$ but with
178 different random phases were performed, and wave parameters are then averaged over the 20
179 realizations and across all the three beams.

180 It is seen that for the unimodal directional spectrum investigated, the wave heights
181 estimated from the along-track profiles are generally in excellent agreement with the true value
182 for all the α simulated (Fig. 1d, α ranges from 0° to 360° with an interval of 1°). Overall, the
183 estimated wave height is lower than the true value by around 2%, which could be attributed to
184 the data filter used in the preprocessing algorithm (Section 2.c). Figure 1f clearly shows that as
185 the separation angle α increases from 0° to 90°, the wavenumber spectrum $F(k)$ becomes
186 more skewed toward the low-wavenumber end, and consequently, the apparent peak
187 wavelength $L_{p,a}$ increases gradually with α. We found that the ratio of the estimated $L_{p,a}$ to

the real L_p still follows the theoretical prediction of Eq. (4) quite well, even for the directionally spread wind sea spectrum analyzed here (Fig. 1e). It is noteworthy that when α reaches 90° and 270°, our simulations suggest that the peak wave energy $F(k_{p,a})$ is about two times the real value, and $L_{p,a}$ is amplified to about one order of magnitude larger than the "ground truth".

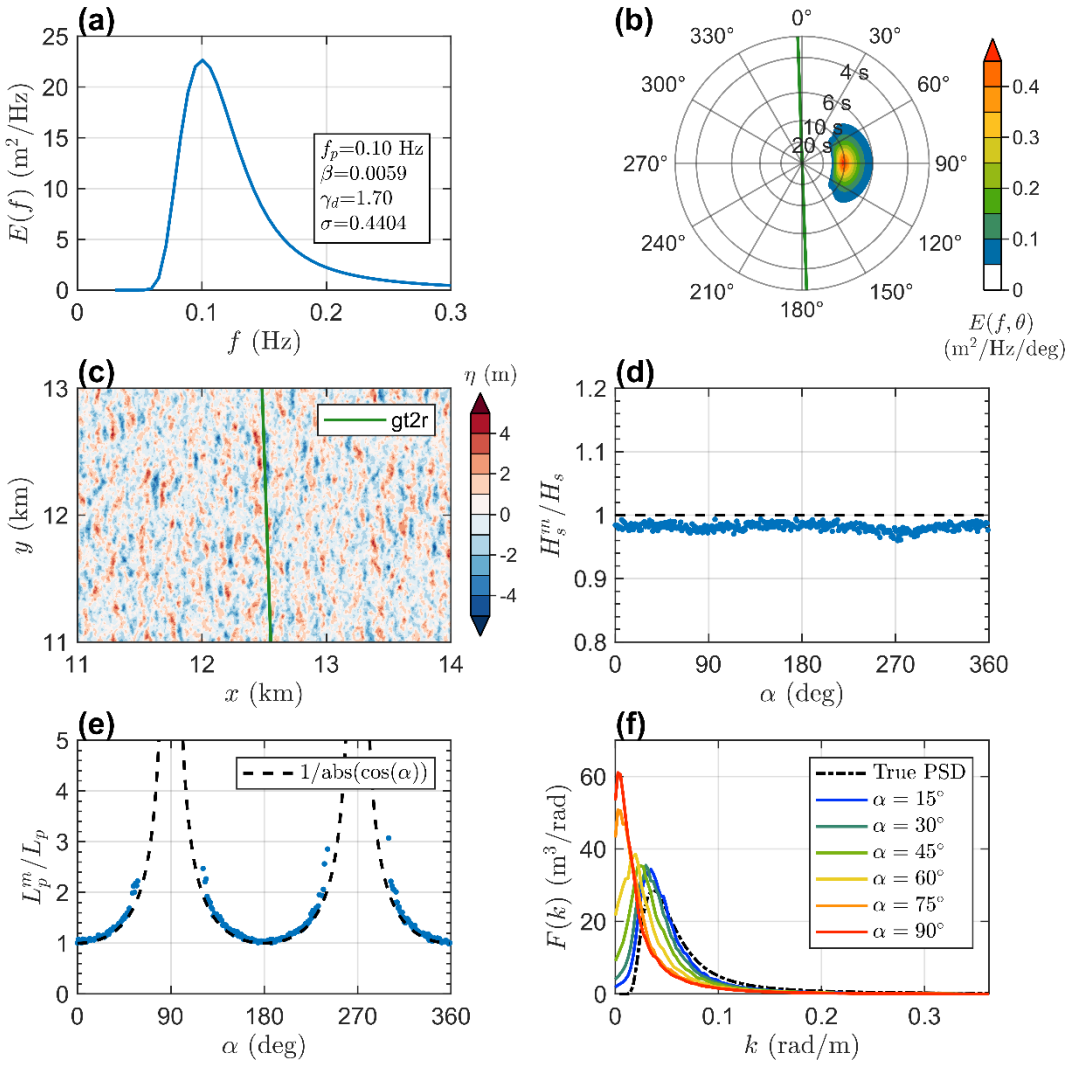

Fig. 1 (a) The frequency spectrum $E(f)$ according to the Donelan's spectral form with U_{10} of 15 m s^{-1} and peak frequency f_p of 0.10 Hz. Other spectral parameters estimated from Eqs. (7-9) are also presented. (b) The directional spectrum $E(f,\theta)$according to Eqs. (5-11). For wave directions, the "coming from" convention is used in this plot. The orientation of the ICESat-2 ground tracks is highlighted as the green solid line. (c) A zoomed-in view (3 km × 2 km domain) of the sea surface elevation $\eta(x,y)$ generated by the WAFO toolbox on a 25 km × 25 km grid. The solid green line highlights one of the ICESat-2 strong beams (i.e., gt2r) used to extract the pseudo along-track surface profiles from the prescribed $\eta(x,y,t)$. The ratio of the "measured" wave height H_s^m and peak wavelength L_p^m (i.e., the apparent peak wavelength $L_{p,a}$) to the true values, as a function of the separation angle α, are shown in (d) and (e), respectively. The black dashed line in (e) highlights the factor $1/\cos\alpha$ as predicted by Eq. (4), where α is the angle between the peak wave direction and the ground track direction. (f) The

wavenumber spectrum $F(k)$ estimated from the along-track observations of η for different α. The black dash-dotted line represents the true wavenumber spectrum ($F(k) = E(f)c_g/2\pi = gE(f)/(8\pi^2 f)$), while other colored solid lines represent the along-track spectrum for α varying from 15° to 90°.

c. Retrieval of wave parameters

In order to determine wave parameters from the ICESat-2 altimetry, we use the strong beam photon heights with medium and high confidence values in the ATL03 ocean data (Fig. 2). We apply ocean tides and a dynamic atmospheric correction including inverted barometer effect to the photon heights using geophysical corrections provided in the ATL03 data set (Markus et al. 2017). In addition, ATL03 provides the photon quality flag (*quality_ph*) and the precise orbit determination and pointing determination flag (*podppd_flag*), the latter of which indicates the quality of the specific geolocation segments. We only retain photon heights with *quality_ph*=0 (to filter out problematic photons due to saturation conditions or instrument effects) and *podppd_flag*=0 or 4 (to filter out photons with a degraded orbit and unrealistic values in ocean segments), while other values indicate potentially problematic photons and segments (Morison et al. 2022). The EGM2008 geoid parameter reported on ATL03 provides reference geoid undulations above WGS-84 reference ellipsoid in a tide-free system (Pavlis et al. 2012). We use the *geoid_free2mean* parameter to convert geoid heights from the tide-free system to the mean-tide system where the permanent tides are included. We then subtract the mean-tide EGM2008 geoid heights from photon heights to obtain the local height of the sea surface above the geoid (Gregory et al. 2019). However, the influence of clouds and changing surface reflectivity can result in gaps or irregularities in ICESat-2 photon retrieval rates, leading to unequally spaced along-track observations of sea surface profiles (Hell and Horvat 2024). For our purpose, we select photon heights within $\pm$20 m of the geoid to remove large height outliers, and choose high-density, continuous photon height profiles only. Given the irregularly-spaced nature of the along-track ICESat-2 raw photon data, we resampled the data at an interval of 5 m using a Piecewise Cubic Hermite Interpolating Polynomial (PCHIP). We then further adopted the Savitzky-Golay (S-G) filter to smooth the signal in order to exclude other potential contaminations from outliers due to photon backscattering and subsurface reflection. The S-G filter is configured with a polynomial order of 5 and a frame length of 7, corresponding to a smoothing window with an along-track distance of 35 m. Figure 2 illustrates one 3-km photon height profile processed by the PCHIP resampling and S-G filtering

procedure, which was obtained from the strong beam GT3R of ICESat-2 (granule: 10120102) on 3 December 2018 near the west coast of US. The profile allows us to obtain fine characteristics of ocean surface waves.

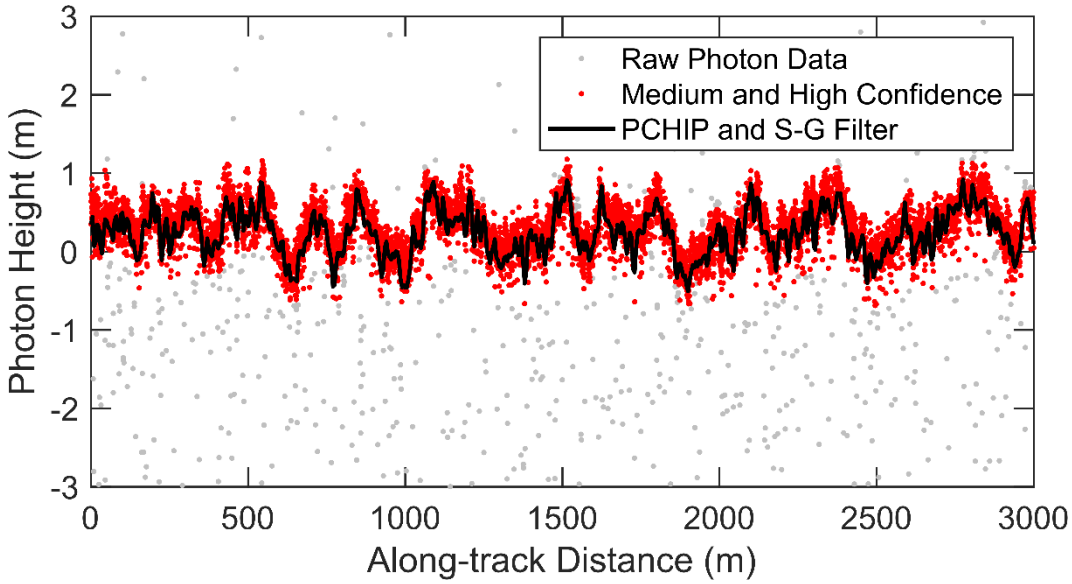

Fig. 2 ATL03 photon height point cloud over a 3-km ocean segment, obtained from one ICESat-2 strong beam GT3R (granule: 10120102 on 3 December 2018). The black line represents the photon height profile after resampling and filtering.

To retrieve ocean wave parameters in deep waters, we divide the preprocessed, continuous, and equally spaced photon height profiles into 20.48-km segments (a total of 4096 5-m sample points) with 50% overlap. Each 20.48-km segment is detrended, and the significant wave height H_s is calculated as four times the standard deviation of the along-track surface profile, i.e., $H_s = 4\sigma_\eta$ (Ardhuin et al. 2019). The wavenumber spectrum $F(k)$ is then estimated with Welch's method (Welch 1967) with the Hamming window and segment lengths of 256 sample points (with 50% overlap). We compute the apparent peak wavenumber $k_{p,a}$ and apparent wavelength $L_{p,a}$ using the parabolic fit around the discrete peak of $F(k)$. With these procedures, we are able to obtain deep-water H_s, $k_{p,a}$ and $L_{p,a}$ at an along-track resolution of 10.24 km. The same methodology is adopted to process coastal observations from the ICESat-2, except that the segment length of 20.48 km is halved owing to the stronger spatial heterogeneity of coastal waves. Consequently, in coastal waters, the wave parameters we estimate are at an along-track resolution of 5.12 km.

d. Validation against buoy data

The validation data for the open ocean and coastal ocean used in this study are obtained from in-situ buoy observations provided by the National Data Buoy Center (NDBC) and the Coastal Data Information Program (CDIP) over the period from October 2018 to August 2021, respectively. The buoy data provide reliable long-term wave measurements, including wave spectra, wave height H_s, peak period T_p, and peak direction θ_p, with temporal resolutions of 1 hour for the NDBC buoys and 30 minutes for the CDIP buoys. Recently the US Army Corps of Engineers (USACE) developed an independent, quality controlled, consistent (QCC) Measurement Archive (Hall and Jensen 2022) that captures the best available NDBC observations with verified metadata. This study uses NDBC buoy data from the USACE QCC Measurement Archive. The NDBC moored buoys are primarily distributed in the open ocean in the North Pacific and West Atlantic, in the vicinity of the Hawaiian Islands, and in the Gulf of Mexico (red squares in Fig. 3a).

In the open ocean, NDBC buoys situated more than 50 km offshore and in waters deeper than 500 m are selected. In the coastal waters, we select CDIP wave buoys within 100 km of the coastline and in water depths less than 300 m. These CDIP moored buoys are distributed in shallow waters off North America and the Hawaiian Islands, with the majority located within 50 km of the coastline (yellow circles in Fig. 3a). With these criteria employed, a total of 81 mooring buoy stations (40 NDBC buoys and 41 CDIP buoys) are obtained for validation, and their locations are summarized in Fig. 3a.

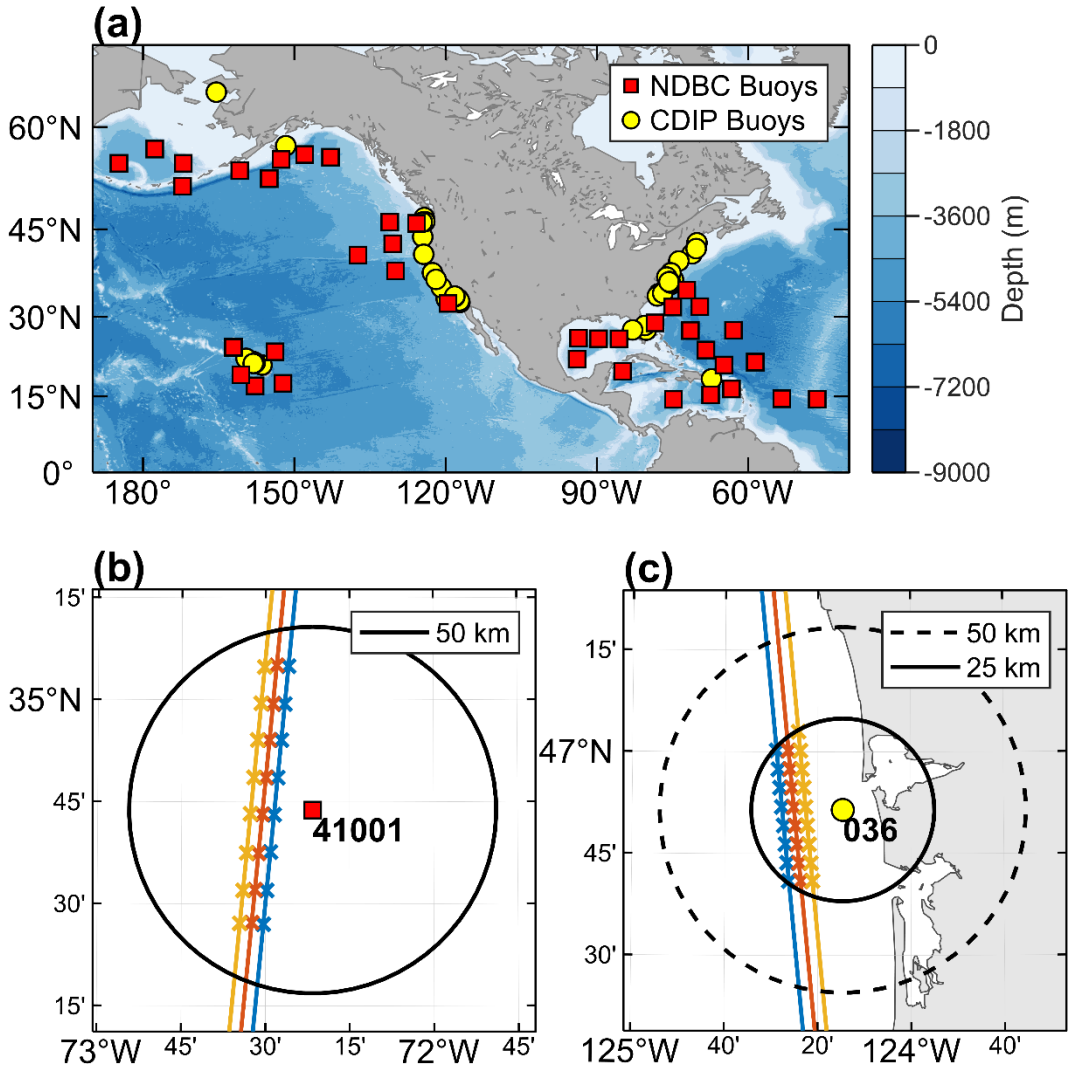

280

281 **Fig. 3** (a) The locations of 40 NDBC (red square) and 41 CDIP (yellow circle) mooring
282 buoy stations used in this study. The NDBC buoys are 50 km offshore with water depths greater
283 than 500 m, and the water depths of the CDIP buoys are all less than 300 m. The schematics
284 for collocating ICESat-2 wave data (cross) with buoy observations in (b) open ocean and (c)
285 coastal ocean are also provided. The black solid circles indicate 50 km and 25 km spatial
286 windows in (b) and (c), respectively. Three strong beams are represented by blue, orange, and
287 yellow lines with descending ground tracks (granule: 01790806 on 7 July 2020) in (b) and
288 ascending ground tracks (granule: 10120102 on 3 December 2018) in (c). The red square
289 represents NDBC buoy (ID: 41001, depth: 4486 m), and the yellow circle represents CDIP
290 buoy (ID: 036, depth: 41 m).

291

292 Because the ICESat-2 and buoys measure wave fields in different ways, one spatially and
293 the other temporally, when collocating measurements from these two platforms, it is essential
294 to assure these observations are comparable in terms of both temporal and spatial scales. For
295 open ocean applications, a typical matching criterion is to use altimetry data within 50 km of a
296 buoy with the time difference less than 30 minutes (Monaldo 1988; Liu et al. 2016).

297 Considering the complexity of the nearshore wave dynamics, a smaller spatial and temporal
298 window (25 km, 15 min) is used in the coastal ocean (Hithin et al. 2015). We interpolate the
299 buoy observations linearly in time to the instant of the ICESat-2 granule, and then spatially
300 average all collocation points near a particular buoy (including wave observations from all the
301 3 ICESat-2 strong beams) by an inverse distance Gaussian weighting scheme (Kessler and
302 McCreary 1993). Based on these criteria, the number of collocated data pairs is 929 in the open
303 ocean and 820 in the coastal ocean. Figure 3b and 3c show the schematic for collocating
304 ICESat-2 wave measurements with buoy observations in the open ocean and coastal ocean,
305 respectively. For example, within 50 km of the NDBC buoy (ID: 41001, depth: 4486 m) located
306 in East Hatteras (Figure 3b), we can obtain 24 valid collocation points from the ICESat-2
307 ground tracks (granule: 01790806) on 7 July 2020, which form one buoy-ICESat-2 collocated
308 pair. In order to facilitate a direct comparison between the wave parameters sourced from
309 ICESat-2 and buoys, the peak period T_p in the buoy data was converted to the corresponding
310 peak wavelength L_p through the dispersion relationship for arbitrary depth, given by:

311 $$L_p = \frac{\mathrm{g}{T_p}^2}{2\pi}\tanh\left(\frac{2\pi d}{L_p}\right), \tag{14}$$

312 where d is the water depth. Given that Eq. (14) is an implicit expression in terms of wavelength,
313 we employ the approximate formula proposed by Fenton (1988) to calculate the peak
314 wavelength observed by buoys. As indicated by Eq. (4) and Fig. 1, the knowledge of peak wave
315 direction θ_p is required to convert the ICESat-2 apparent peak wavelength $L_{p,a}$ to the "real"
316 peak wavelength, that is,

317 $$L_p = L_{p,a}\cos\alpha\,, \tag{15}$$

318 where α, as mentioned in Section 2.b, is the angle between the peak wave direction and the
319 ground track direction. In the following sections, we first use the buoy-measured peak wave
320 direction for accomplishing this conversion (Section 3). The results for L_p estimated directly
321 from ICESat-2 strong and weak beams based on the cross-spectral analysis are presented in
322 Section 4.b.

323 Four statistical parameters are used to quantify the comparisons of ICESat-2 wave data
324 with in-situ buoy observations. These include the bias (b), root mean square error (RMSE, ε),
325 correlation coefficient (ρ), and scatter index (SI), which can be expressed as follows:

$$b = \frac{1}{N}\sum_{i=1}^{N}(x_i - y_i), \tag{16}$$

$$\varepsilon = \sqrt{\frac{1}{N}\sum_{i=1}^{N}(x_i - y_i)^2}, \tag{17}$$

$$\rho = \frac{\sum_{i=1}^{N}(x_i - \bar{x})(y_i - \bar{y})}{\sqrt{\sum_{i=1}^{N}(x_i - \bar{x})^2 \sum_{i=1}^{N}(y_i - \bar{y})^2}}, \tag{18}$$

$$\mathrm{SI} = \frac{\sqrt{\frac{1}{N}\sum_{i=1}^{N}[(x_i - \bar{x}) - (y_i - \bar{y})]^2}}{\bar{y}}, \tag{19}$$

where x and y represent ICESat-2 data and buoy data, respectively, the upper bar denotes the statistical average, and N is the number of collocated data pairs.

3. Results

a. Wave parameters in open oceans

Figure 4a presents the comparison of significant wave height H_s between ICESat-2 and NDBC deep-water buoys. For wave height, the ICESat-2 measurements are in excellent agreement with NDBC buoy observations. With the criteria of 50 km and 30 min for the spatio-temporal separation, a total of 929 collocations are obtained, exhibiting a marginal bias (2 cm), a fairly low RMSE ($\varepsilon = 0.16$ m), a very high correlation ($\rho = 0.98$) and a low scatter index ($SI = 0.09$). Our H_s results are consistent with previous studies that compared ICESat-2 with ERA-5 reanalysis and WAVEWATCH III (hereafter WW3) model in the open ocean, corresponding to a root mean square error of 0.38 m and 0.34 m, respectively (Klotz et al. 2020; Yu et al. 2021). We further note that the H_s accuracy shown here is also comparable to that of radar altimeters (Zieger et al. 2009; Liu et al. 2016; Ribal and Young 2019). To analyze the differences between the H_s measurements from ICESat-2 and NDBC for varying sea states, we grouped the buoy H_s shown in Fig. 4a into 1-m bins and calculated the corresponding bias (b) and scatter index (SI) for each bin (any bins with at least 3 collocated data pairs), as illustrated in Fig. 4c. The results show that the mild sea states (e.g., $H_s < 2m$) are unbiasedly detected by ICESat-2. As sea states become more severe ($H_s > 3$ m), ICESat-2 shows an

underestimation of 0.1–0.2 m. The scatter index exhibits little variations with increasing H_s and is under 0.11 for the whole range analyzed.

Figure 4b presents a scatter plot of peak wavelength L_p between ICESat-2 and NDBC buoys. The Welch's method we use for obtaining $F(k)$ from ICESat-2 profiles employs a segment length of 256 sample points (Section 2.c), thus the lowest wavenumber that could be resolved is $1/(256 \times 5m) = 1/1280$ m^{-1}. Any ICESat-2 measurements with an apparent peak wavelength greater than this cut-off value (i.e., 1280 m) was excluded from our analysis. We note that there are a large number of ICESat-2 $L_{p,a}$ measurements exceeding this value owing to the "distorting" effect of the along-track sampling (Section 2.b). As a result, the total number of collocation pairs for L_p is considerably lower than that for H_s.

The L_p recovered from ICESat-2 using Eq. (15) is in good agreement with buoy observations, but the comparison is more scattered than the H_s results. The bias is about 8 m and the RMSE is 76 m. The correlation coefficient reduces to 0.75 and the SI increases to 0.49. For comparison, Yu et al. (2021) compared their ICESat-2-estimated peak wavelength against a WW3 wave hindcast and reported a RMSE of 151 m. The peak period of the NDBC buoy data shown in Fig. 4b is between 3.09 s and 19.05 s, thus the corresponding peak wavelength spans a fairly wide range from 14.8 m to 566 m. Figure 4d gives the bias and SI between L_p measurements from ICESat-2 and NDBC as a function of buoy L_p (100-m bin). We find that for relatively short waves ($L_p < 100$ m, corresponding to $T_p < 8$ s), ICESat-2 overestimates L_p by approximately 20 m, with a SI considerably greater than 0.5. When the buoy L_p exceeds 200 m, ICESat-2 underestimates L_p with a gradually decreasing SI.

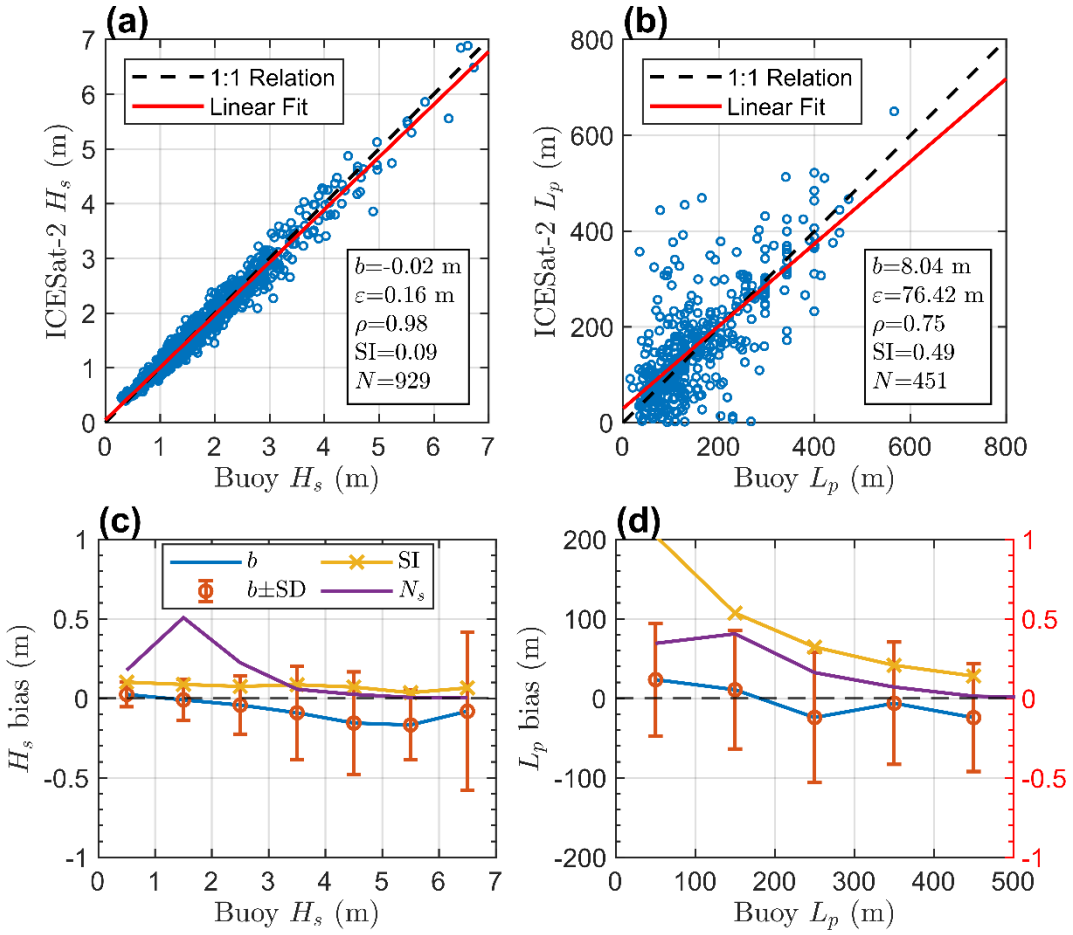

370

371 **Fig. 4** Comparisons of (a) significant wave height H_s and (b) peak wavelength L_p between
372 ICESat-2 and NDBC buoys in the open ocean. The apparent wavelength observed by ICESat-
373 2 has been corrected to the actual wavelength using Eq. (15) with the input of buoy-observed
374 peak wave direction. The black dashed line represents the 1:1 relationship and the red line
375 represents a simple linear fit. Four statistical parameters and the total number of collocated data
376 pairs are also provided. The biases of H_s and L_p measurements derived from ICESat-2 as a
377 function of buoy-measured H_s and L_p are presented in panels (c) and (d), respectively, along
378 with the standard deviation, scatter index (SI) and the rescaled N_s (number of collocated pairs
379 in each bin normalized by the total number of collocated data pairs, N).

380

381 Figure 5 shows a closer inspection of the performance of ICESat-2 wave measurements, in
382 terms of SI, at each NDBC deep-water buoy. For H_s, ICESat-2 has a SI of less than 0.1 at the
383 majority of NDBC buoys in both the Pacific and Atlantic Oceans (Fig. 5a). For L_p, the SI is
384 noticeably larger and could be above 0.5 in the Gulf of Mexico and the western Atlantic (Fig.
385 5b).

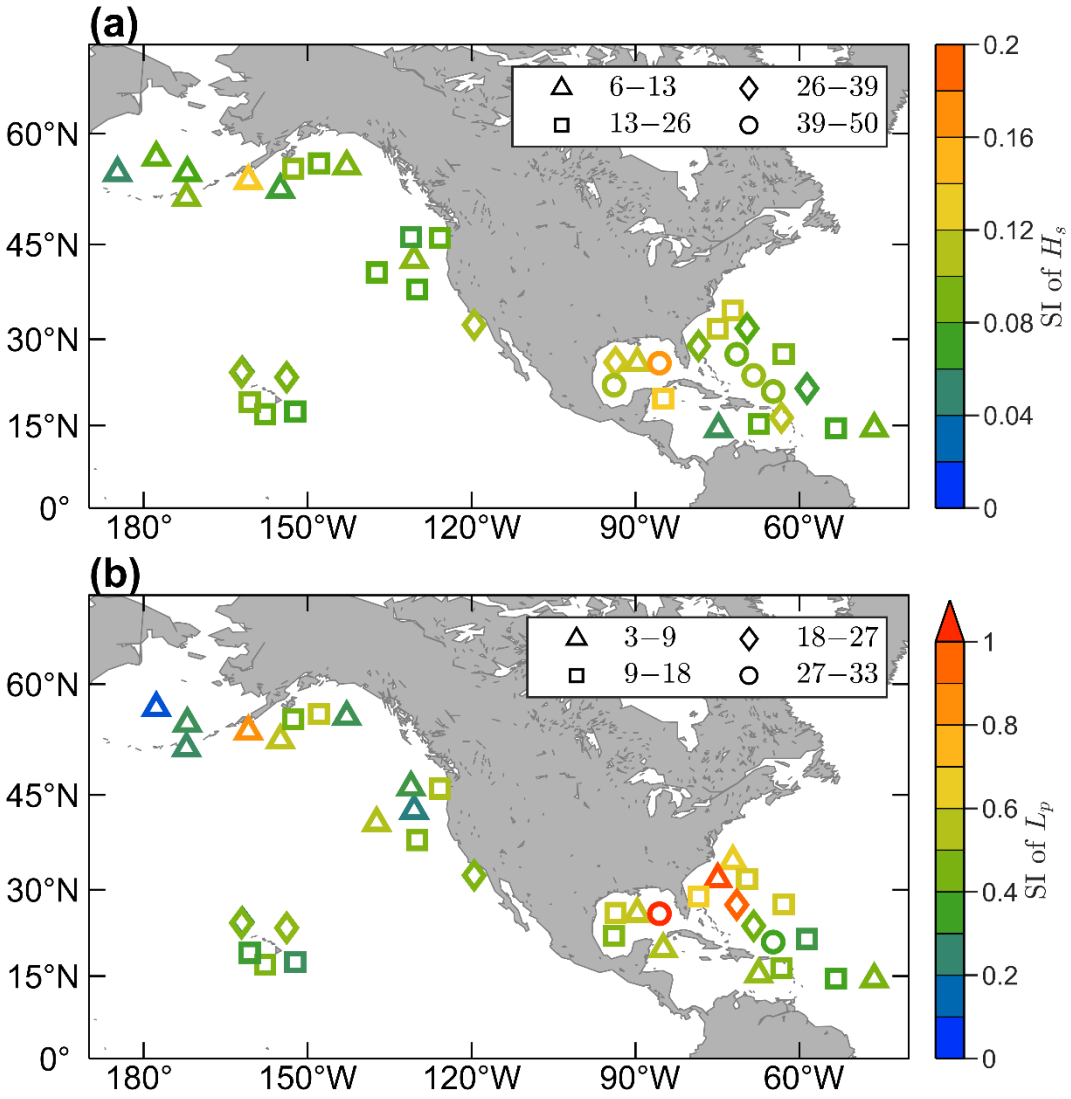

Fig. 5 The scatter index (SI) of ICESat-2 (a) H_s and (b) L_p at different NDBC buoys in the open ocean. Different marker symbols (triangle, square, diamond, and circle) highlight the total number of collocated data pairs at individual buoys. The color of the marker indicates the value of SI.

b. Wave parameters in coastal waters

As mentioned in Section 2.d, ICESat-2 wave observations in the coastal ocean are validated using data from CDIP wave buoys deployed off the coasts of North America and the Hawaiian Islands. These wave buoys are deployed in shallow waters (less than 300 m), with offshore distances ranging from 287 m to 91.7 km. For ICESat-2 ground tracks that intersect with the land, we only retain a subset of the along-track data that are more than 3 km away from the coastline.

Figure 6a presents the comparison of H_s between ICESat-2 measurements and CDIP buoy observations. The accuracy of the ICESat-2 H_s reduces slightly when moving from deep waters to coastal regions. Nonetheless, it is still in remarkable agreement with CDIP buoy data. A total of 820 collocations yields a 3-cm bias and a RMSE of 0.26 m. The correlation coefficient is higher than 0.9 and the SI is around 0.2. Our H_s results in the coastal ocean are similar to those of Dietrich et al. (2023) and are comparable to the performance of SARAL/AltiKA altimeter near the coast (Hithin et al. 2015). Figure 6c shows that ICESat-2 overestimates low sea conditions ($H_s < 1$ m) by roughly 9 cm in the coastal ocean and then underestimates larger wave heights by 0.1–0.2 m, similar to the results shown in Fig. 4c. Again, the SI is relatively stable with H_s except that SI is slightly larger for low wave heights.

Figure 6b presents a scatter plot of L_p between ICESat-2 measurements and CDIP buoy observations in the coastal ocean. Similar to the deep-water results, the performance of the ICESat-2 L_p in coastal waters is also less favorable, and the error metrics are comparable to their deep-water counterparts ($b = 17.43$ m, $\varepsilon = 78.12$ m, $\rho = 0.71$, $SI = 0.56$). The peak period of the CDIP buoy data given in Fig. 6b is between 1.74 s and 18.18 s, with a corresponding peak wavelength between 4.7 m and 499.4 m. In Fig. 6d, we find that for shorter wavelengths ($L_p < 100$ m) observed by the CDIP buoys, ICESat-2 L_p shows a more pronounced overestimation ($b = 40$ m, $SI > 1$). When the peak wavelength of the buoys exceeds 200 m, the SI gradually decreases and falls below 0.5, indicating that the L_p retrieved by ICESat-2 may have a smaller error for long propagating swells in both open oceans and coastal waters (Figs. 4d, 6d).

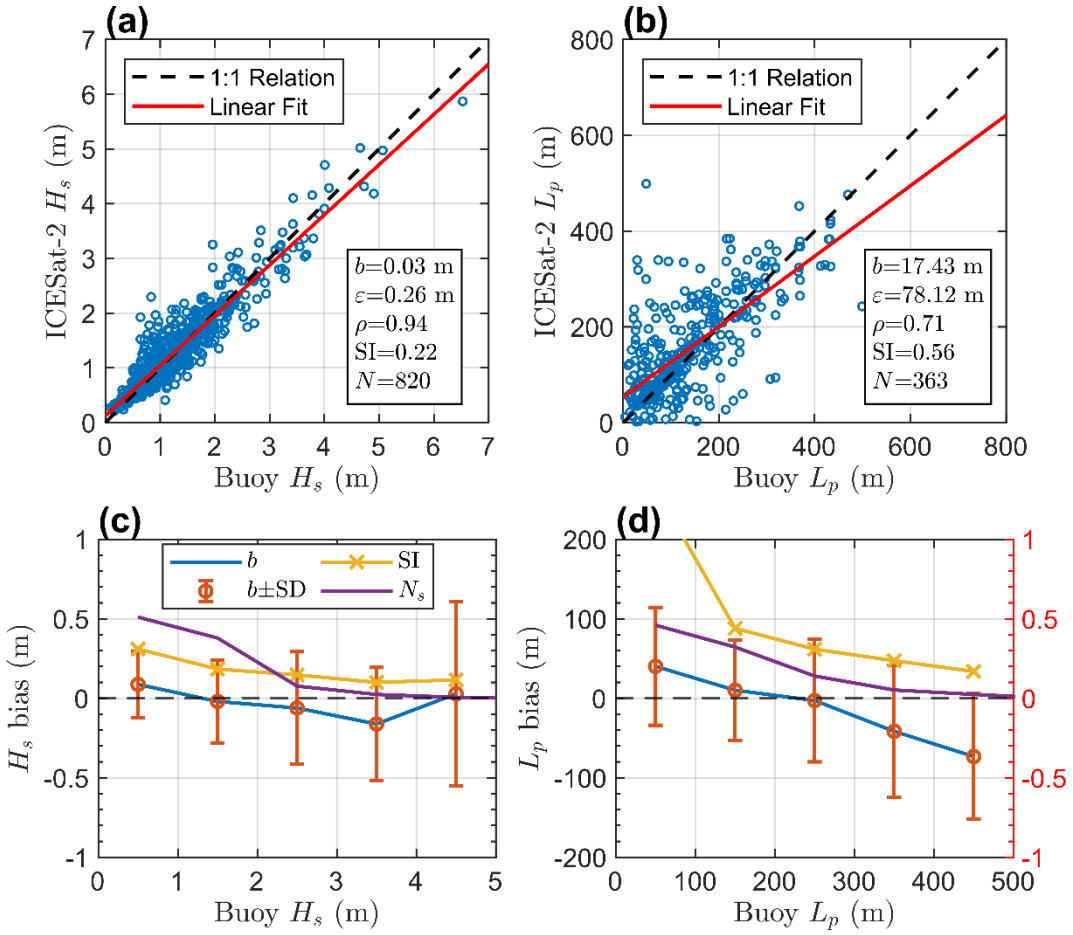

420

421 **Fig. 6** Same as Fig. 4 but for the comparison of (a) H_s and (b) L_p between ICESat-2 and
422 CDIP coastal buoys.

423

424 The SI of H_s and L_p at various CDIP buoy locations in the coastal ocean is presented in Fig.
425 7. In the majority of shallow and nearshore regions, the SI of H_s is less than 0.2 (Figs. 7a-b).
426 However, there are several CDIP buoys that are close to land or sheltered bays with larger
427 scatter index ($SI > 0.3$). For example, the maximum SI of H_s is found at the CDIP buoy 143
428 (depth: 9.8 m) located off the coast of Cape Canaveral, Florida, with an offshore distance of
429 approximately 5 km (Fig. 7b). The deterioration of ICESat-2 H_s may be attributed to the
430 determination of surface signal photons, especially at water depths less than 50 m and within
431 10 km offshore. When water depths are too shallow or too close to the shoreline, the confidence
432 assessment and surface type classification provided by ATL03 data set are not always reliable,
433 which may include signal photons below the surface, such as subsurface scattering and seafloor
434 signal photons (Ma et al. 2020). Due to the relatively large spatial gradient of H_s in the coastal
435 ocean, the removal of ICESat-2 along-track data within 3 km of the coastline may also
436 introduce a bias in the CDIP-ICESat-2 comparison owing to the preference of the seaward

sampling by ICESat-2. In Fig. 7c, although the SI of ICESat-2 L_p is small at some of the coastal buoys, it is still larger than 1 at the buoys located in bays, shallows and offshore beaches (Fig. 7d).

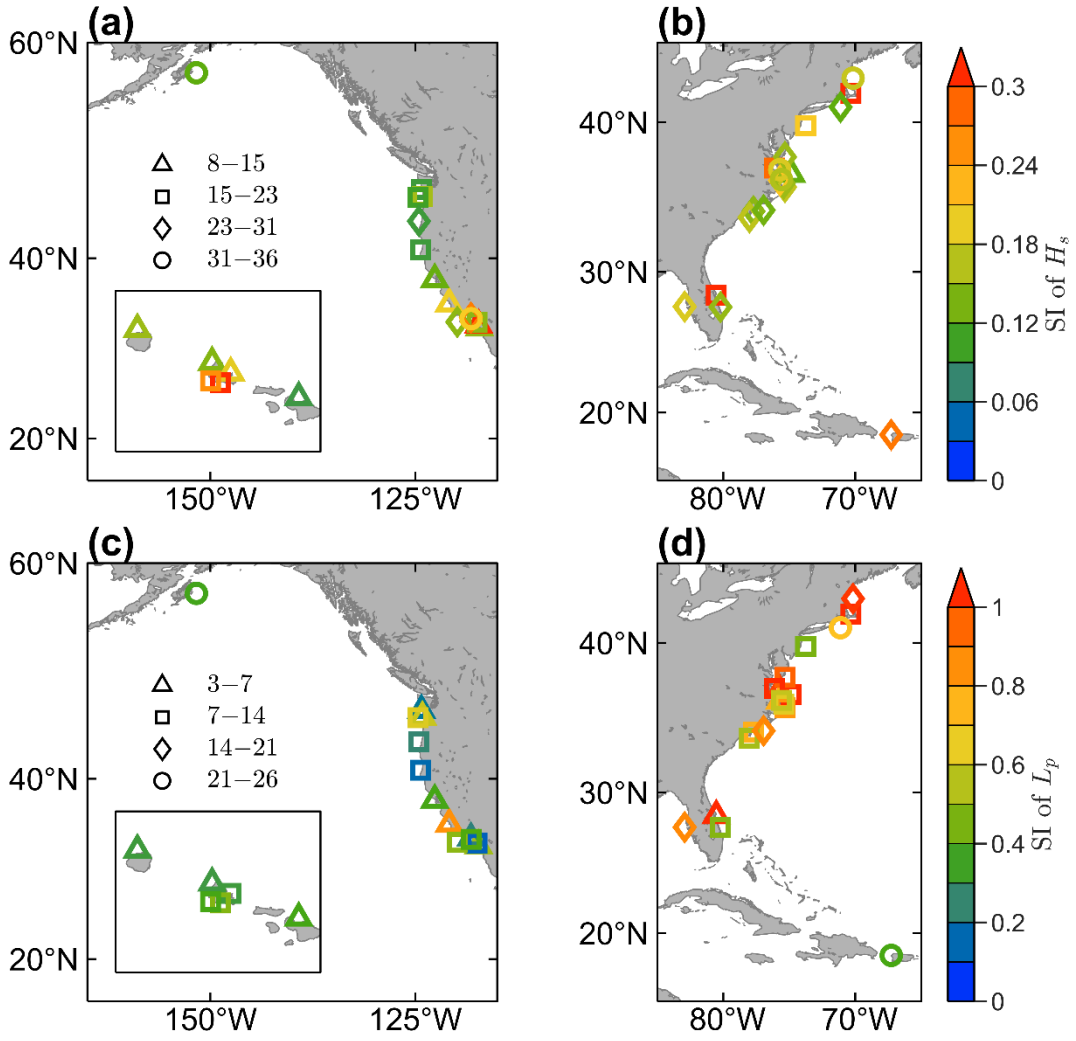

Fig. 7 The scatter index (SI) of ICESat-2 (a-b) H_s and (c-d) L_p at different CDIP buoys in coastal waters. The insets in (a, c) present results at CDIP buoys near Hawaiian Islands. Different marker symbols (triangle, square, diamond, and circle) represent the total number of collocated data pairs at individual buoys. The color of the marker indicates the value of SI.

4. Discussion

a. Mixed sea states

In the previous sections, we estimated the apparent peak wavelength $L_{p,a}$ from the ICESat-2 along-track wavenumber spectrum and then corrected it to the actual wavelength L_p according to Eq. (15). This geometric correction appears to perform well under unimodal sea

451 states, as demonstrated by our WAFO simulations (Fig. 1e). However, the relatively large
452 errors in the ICESat-2 recovered L_p relative to buoy measurements, as shown in Figs. 4 and 6,
453 indicate that the correction of Eq. (15) might not be appropriate/suitable in real oceans, in which
454 sea states are frequently mixed by local wind seas and swells propagating from remote stormy
455 regions (Hanson and Phillips 2001; Liu et al. 2021).

456 To investigate how the along-track sampling and Eq. (15) work in mixed sea states, we
457 repeat the WAFO numerical simulations shown in Fig. 1 for more complex, crossing seas here.
458 The Torsethaugen bimodal spectral model (Torsethaugen and Haver 2004; Brodtkorb et al.
459 2000) is adopted to construct the frequency spectrum $E(f)$. Specifically, $E(f)$ is composed of
460 a wind sea spectrum with wave height of 4.61 m and peak period of 8 s, and a swell spectrum
461 with wave height of 3.71 m and peak period of 14 s, resulting in a bimodal, wind sea-dominated
462 spectrum with a total wave height of 6 m and peak period of 8 s (Fig. 8a). We further calculate
463 the directional spectrum $E(f,\theta)$ according to Eqs. (10-11) for the wind sea and swell systems,
464 respectively, forcing that the peak direction of the low-frequency swell system is always
465 perpendicular to that of the local wind sea system. Figure 8b, as an example, shows a crossing
466 sea with the wind sea system coming from the east ($\theta_{p,w} = 90°$) and the swell coming from
467 the south ($\theta_{p,s} = 180°$). A zoomed-in view of the instantaneous sea surface elevation $\eta(x,y,t)$
468 corresponding to this specific $E(f,\theta)$ is given in Fig. 8c, which is apparently more irregular
469 than that in Fig. 1c.

470 The wave parameters estimated from pseudo ICESat-2 along-track profiles under crossing
471 seas, as a function of α (the separation angle between ICESat-2 ground track and θ_p at an
472 interval of 5°) are checked in Figs. 8d-f. Consistent with unimodal cases (Fig. 1d), the accuracy
473 of ICESat-2 wave height H_s is still very high for crossing seas and only changes marginally
474 with α (Fig. 8d). However, inspection of the along-track wavenumber spectra $F(k)$ shows a
475 fairly complex pattern (Fig. 8f). For small α (e.g., $\alpha = 12°$), the low-frequency swell peak is
476 heavily distorted and becomes ill-defined. As α increases, it seems that the initial wind sea
477 peak is gradually smeared out (or alternatively, skewed towards low frequencies), and
478 consequently the "distorted" $F(k)$ degrades to be unimodal and "swell-dominated" with its
479 peak located in the vicinity of the original swell peak. With such heavily distorted $F(k)$, the
480 correction factor, $1/\cos\alpha$, for recovering peak wavelength L_p becomes meaningless for these
481 crossing seas, as revealed in Fig. 8e (black crosses for $L_{p,a}/L_{p,w}$, where $L_{p,w}$ is the real wind
482 sea peak wavelength and hence also the peak wavelength for the total spectrum). Interestingly,

for most cases, the apparent wavelengths from ICESat-2 seem conform to $L_{p,a} = L_{p,s}/\cos\alpha'$, where $L_{p,s}$ is the real peak wavelength for the swell system (Fig. 8a), and α' refers to the separation angle between ICESat-2 tracks and the swell peak direction $\theta_{p,s}$.

These results clearly illustrate the difficulties in recovering peak wavelength from ICESat-2 along-track surface elevations under mixed sea states. Even for occasions when the directional spectra are known a priori, it becomes challenging to attribute the apparent peak wavelengths to the true values (e.g., which α should be used for the conversion in Eq. (15)). A more complicated example is further provided in Fig. S4 of the supporting online material (SOM), where a three-modal wave spectrum observed by NDBC buoy 46047 (one wind sea system and two swell systems) is investigated. For this mixed sea state, the estimated peak wavelength based on Eq. (15) is 209 m, far different from the buoy-measured value (119.5 m).

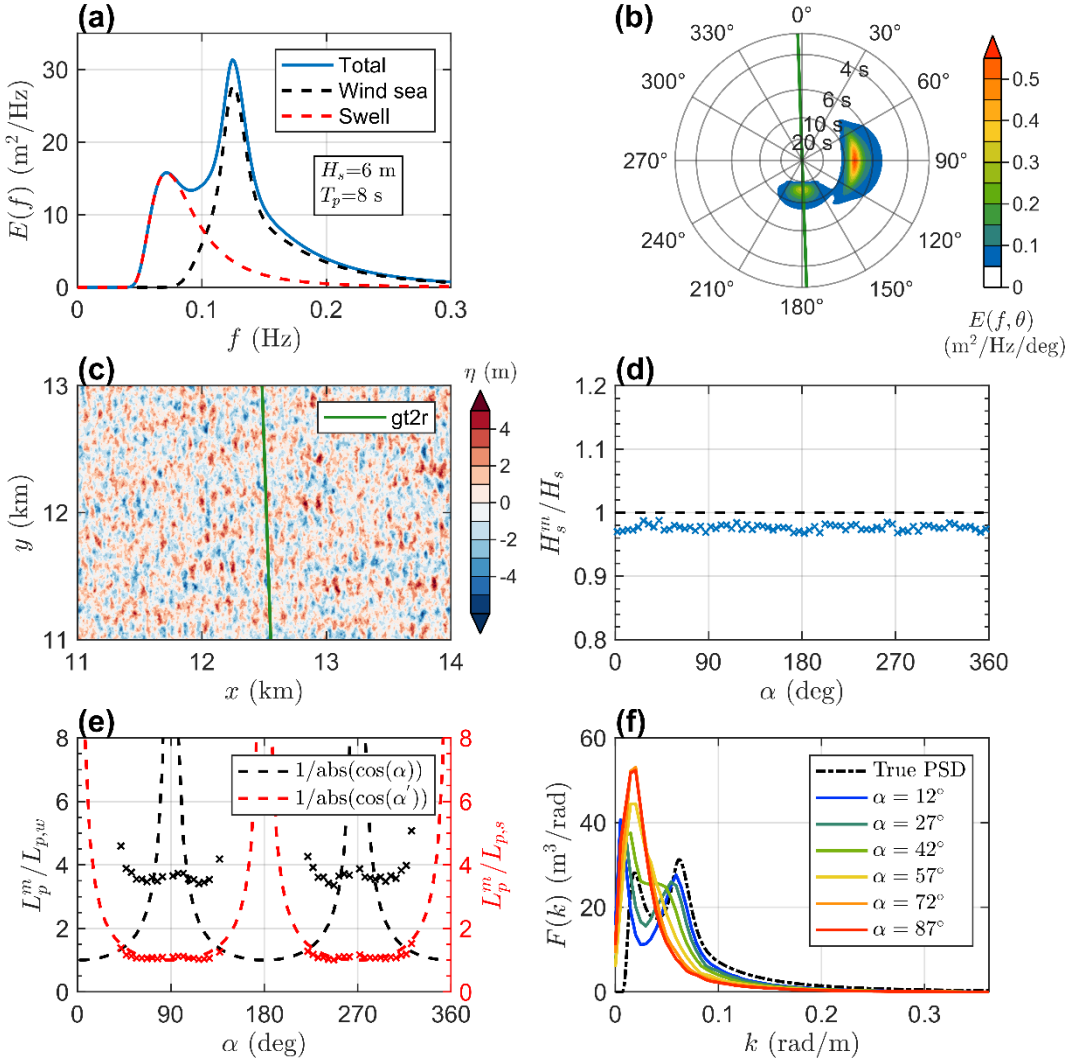

Fig. 8 Same as Fig. 1 but for (a) the Torsethaugen bimodal spectrum $E(f)$ with$H_s = 6$ m and $T_p = 8$ s, which can be decomposed into the wind sea spectrum (black dashed line) and

the swell spectrum (red dashed line), respectively. (b) The directional spectrum $E(f,\theta)$ built for the Torsethaugen bimodal spectrum $E(f)$ with the directional spreading function according to Eqs. (10-11). Specifically, the peak wave directions are chosen as 90° and 180° for the wind sea and swell systems, respectively. (e) The ratio of the "measured" peak wavelength L_p^m to the wind sea peak wavelength $L_{p,w}$ and the swell peak wavelength $L_{p,s}$, as a function of α (the separation angle between ICESat-2 ground track and peak wave direction), are shown as black and red crosses, respectively. The black (red) dashed line highlights the factor $1/\cos\alpha$ ($1/\cos\alpha'$), where α (α') is the angle between the track orientation and the wind sea (swell) peak direction.

b. Peak wave direction

To this point, we have focused on significant wave height and peak wave length retrieved from ICESat-2 in open ocean and coastal waters with the input of buoy-measured peak wave direction. Yu et al. (2021) suggested that the peak wave direction could be approximately determined through the clear coherence between the strong and weak beams spaced at a cross-track distance of 90 m in each ICESat-2 beam pair. In the case of high coherence within ICESat-2 strong/weak beam pairs, we can obtain the relative phase shift between the two along-track elevation profiles by the cross-spectral analysis, which subsequently can be used to estimate the peak wave direction θ_p, though with a 180° ambiguity (Yu et al. 2021; Dietrich et al. 2023). We investigate the accuracy of θ_p estimated from the strong and weak beam pairs in this subsection (theory and details of estimating θ_p based on the cross-spectral analysis is summarized in section S1 of the SOM).

Through the WAFO simulations for unimodal and bimodal spectra, we found that i) for the unimodal cases shown in Fig. 1, the peak direction θ_p estimated from the cross-spectral analysis and according to Eqs. (S5, S6) is in excellent agreement with the prescribed values (Fig. S2f); ii) but under mixed sea states (Fig. 8), similar to the estimated peak wavelength, the estimated θ_p could deviate from actual values considerably (Fig. S3d).

During the early science operations of ICESat-2, only strong beam data over the oceans and weak beam data in near-coastal zones were routinely telemetered, and it was not until June 2021 that routine global collection of weak beam data began (Neumann et al. 2022). We select high-density and continuous strong and weak beam pairs from the existing ICESat-2 data, and calculate θ_p with an along-track resolution consistent with H_s and L_p. The collocation method described in Section 2.d is also used. As a result, we obtain 52 collocated data pairs in the open

ocean and 395 collocated data pairs in the coastal ocean for the duration considered (Oct 2018 – Aug 2021).

To quantify the accuracy of the estimated θ_p, we utilize the angular bias defined by Bowers et al. (2000):

$$b_a = \begin{cases} tan^{-1}\left(\frac{S}{C}\right), & if\ S > 0, C > 0 \\ tan^{-1}\left(\frac{S}{C}\right) + \pi, & if\ C < 0 \\ tan^{-1}\left(\frac{S}{C}\right) + 2\pi, & if\ S < 0, C > 0 \end{cases} \quad (20)$$

where S and C are calculated from the directional differences $\Delta\theta = \left|\theta_x - \theta_y\right|$ by

$$S = \sum_{i=1}^{n} sin(\Delta\theta_i)\,, \quad (21)$$

$$C = \sum_{i=1}^{n} cos(\Delta\theta_i)\,, \quad (22)$$

and the circular correlation defined by Hanson et al. (2009):

$$\rho_c = \frac{\sum_{i=1}^{n} sin(\theta_x - \overline{\theta_x})\, sin\left(\theta_y - \overline{\theta_y}\right)}{\sqrt{\sum_{i=1}^{n}[sin(\theta_x - \overline{\theta_x})]^2 \sum_{i=1}^{n}\left[sin\left(\theta_y - \overline{\theta_y}\right)\right]^2}}. \quad (23)$$

The RMSE is also calculated by Eq. (17) with an angle difference.

Figure 9a presents a scatter plot of θ_p between ICESat-2 and NDBC buoys in the open ocean. Owing to the 180° ambiguity, the ICESat-2 peak wave direction could be either θ_p or $\theta_p + 180°$. For comparison, we choose one of these two values that is closer to the collocated buoy-measured one. Directional statistics show that ICESat-2 θ_p roughly corresponds to the peak wave direction observed by the NDBC buoys. The angular bias b_a is 28.5°, the RMSE ε is about 40° and the circular correlation ρ_c is 0.71. For the coastal ocean, we obtained similar results with $b_a = 28°$, $\varepsilon = 41°$ and $\rho_c = 0.68$ (Fig. 9c). As we found, the larger errors of ICESat-2 θ_p can be attributed to the presence of multimodal sea states (e.g., Figs. S4e-f). The coherence between ICESat-2 strong and weak beams is crucial for determining the wave directionality, but it may be also affected by the physical interactions in coastal environments, such as wave refraction by coastal features, wave reflections from the coast, and velocity

variation caused by bathymetry (Dietrich et al. 2023). The ICESat-2 peak wavelength L_p converted from $L_{p,a}$ by Eq. (15) but with the ICESat-2 θ_p is compared against buoy observations in Figs. 9 (b) and (d) for open and coastal waters, respectively. Similar to the results in Section 3, the comparison is relatively scattered but the ICESat-2 L_p represent a good indication of buoy-observed values.

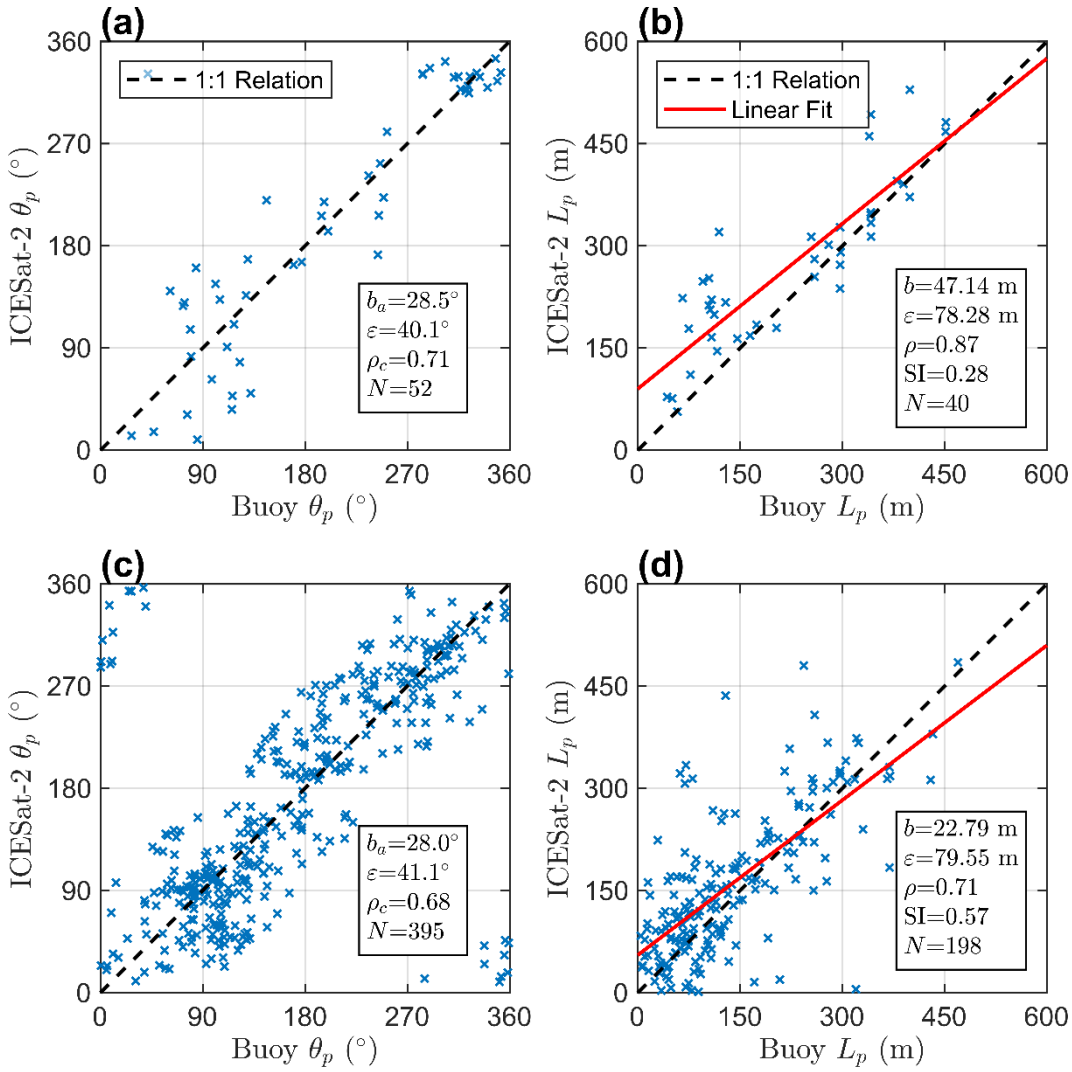

Fig. 9 Comparisons of (a) peak wave direction θ_p estimated from ICESat-2 measurements according to Eqs. (S5, S6) and (b) peak wavelength L_p corrected by ICESat-2 θ_p using Eq. (15) with respect to buoy observations in the open ocean. (c-d) Same as (a-b) but for the coastal ocean. The black dashed line represents the 1:1 relationship and the red line represents a simple linear fit. Directional statistics (angular bias b_a, RMSE ε and circular correlation ρ_c) and the total number of collocated data pairs are also provided.

c. Comparison against spectral wave models

As a complemental analysis, in this subsection, we compare the ICESat-2 wave parameters against wave data sourced from the global wave hindcast of Liu et al. (2021) based on the spectral wave model WAVEWATCH III (The WAVEWATCH III® Development Group, 2019; hereafter WW3). The global hindcast used the observation-based source term package ST6 (Liu et al. 2019), was forced by the ERA5 reanalysis winds (Hersbach et al. 2020) and was archived on a $0.25° \times 0.25°$ grid at 3-hourly intervals. As a test-case, we collected ICESat-2 deep-water data during January 2022 in the South China Sea (SCS), and calculated wave parameters (H_s, L_p, θ_p) with an along-track resolution of 10.24 km. Note that the ICESat-2 L_p presented here are based on Eq. (15) with the modelled peak wave direction. The ICESat-2 L_p estimated from the ICESat-2 θ_p is checked in Fig. S5.

Figure 10a presents the descending ground track (granule: 04761407) of ICESat-2 strong beam gt1l in the SCS at 11:05 UTC 22 January 2022 (the magenta solid line), with the wave field sourced from the WW3 hindcast of Liu et al. (2021). It can be observed that on 22 January, ocean waves originating from the northeast, with a peak period T_p of about 9 s ($L_p \approx 126$ m), propagated toward the eastern coast of the Indo-China Peninsula and passed through the descending track of ICESat-2 at an angle between 30° and 60°. Figure 10b shows the variations of ICESat-2 wave parameters (H_s, L_p and θ_p) along the descending track on 22 January, which are consistent with the WW3 hindcast.

The comparisons of ICESat-2 wave parameters against the WW3 hindcast over the entire January 2022 in the SCS are shown in Figs. 10c-e. Consistent with the comparisons against buoy measurements, the ICESat-2 H_s agrees very well with the WW3 hindcast (a correlation coefficient of 0.85 and a SI of 0.17), but the comparisons for L_p and θ_p are less favorable. Specifically, the correlation coefficient for L_p is less than 0.4, partly owing to the presence of some unrealistically large wave length (above 300 m), which is a typical sign of distorted wave spectra owing to the along-track sampling (e.g., Figs. 1 and 8). The correlation coefficient for peak direction θ_p is less than 0.5 as well. It is noted that short wavelengths of surface waves ($L_p < 90$ m) may lead to weak coherence between the strong and weak beams, which can affect the cross-spectrum and the derived θ_p.

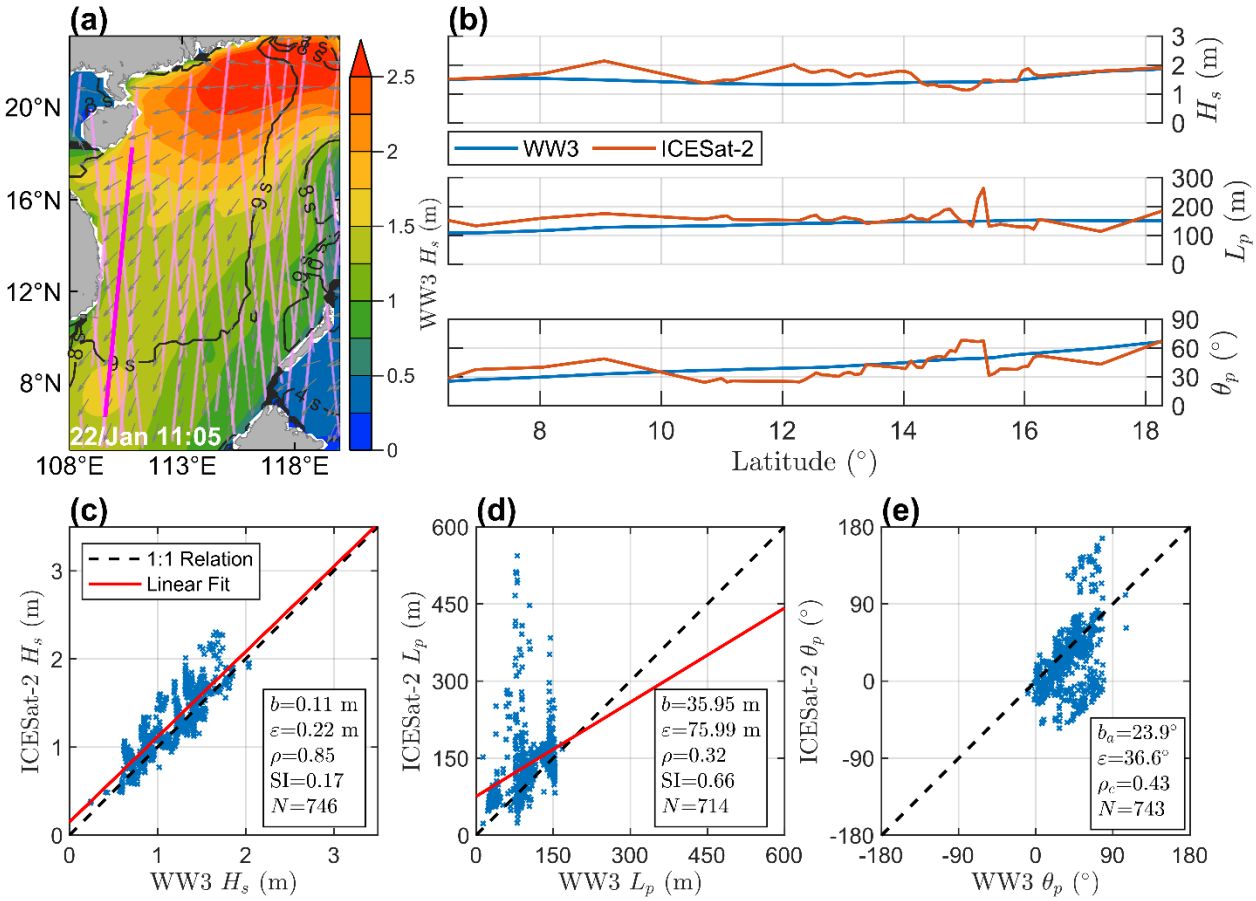

Fig. 10 (a) Spatial distribution of WW3 wave parameters at the instant of the ICESat-2 granule 04761407 in the South China Sea (SCS), with shaded contours representing significant wave height H_s, black contours representing peak period T_p and gray arrows representing peak wave direction θ_p (coming from). The magenta solid line highlights ICESat-2 strong beam gt1l with the descending ground track (granule: 04761407 on 22 Jan 2022). The other light magenta lines represent all granules collected in the SCS during January 2022. (b) The variations of ICESat-2 wave parameters (H_s, L_p, θ_p; orange lines) along the descending track (the magenta ICESat-2 track shown in panel a), with WW3 simulations as a reference (blue lines). Comparisons of (c) H_s, (d) L_p and (e) θ_p between ICESat-2 and WW3 during the whole month of January 2022 in the SCS. The black dashed line represents the 1:1 relationship and the red line represents a simple linear fit. Statistical parameters and the total number of collocated data pairs are also provided.

5. Conclusions

The ICESat-2 ATL03 photon data provides high-resolution profiles of ocean surface, from which we can obtain quantitative estimates of wave parameters, including significant wave height H_s, peak wavelength L_p and peak wave direction θ_p. The much smaller footprint (~11 m in diameter) of ICESat-2 beams compared to radar altimeters enables it as a unique sensor for measuring ocean surface waves. However, owing to the 1D along-track sampling, the

wavelength estimated from ICESat-2 is typically not the actual wavelength since the ICESat-2 ground tracks are generally not perfectly aligned with the direction of wave propagation. The along-track spectrum of ICESat-2 is sensitive to the angle separation between the ground tracks and dominant wave directions (Figs. 1 and 8), and the recovery of the actual wavelength typically requires additional auxiliary information of wave directions (Eq. 15).

In this paper, we retrieved wave parameters from ICESat-2 along-track surface profiles over the period from October 2018 to August 2021. We then validated the ICESat-2 wave parameters using in-situ buoy observations in both open oceans and coastal waters (i.e., the NDBC and CDIP buoys). The results suggest that wave heights from ICESat-2 are in excellent agreement with buoy observations, with a RMSE of 0.16 (0.26) m in open oceans (coastal waters) and a correlation coefficient higher than 0.9 (Figs. 4 and 6). The comparisons between ICESat-2-derived other parameters (namely peak wave length L_p and peak wave direction θ_p) and buoy observations are more scattered, but the ICESat-2 estimates of L_p and θ_p remain generally useful for coastal and oceanic applications, showing correlation coefficients of approximately 0.7 with buoy observations (Figs. 4, 6, 9). Comparisons against wave hindcasts yield similar results regarding on the accuracy of ICESat-2 wave parameters (Fig. 10).

Through WAFO numerical simulations (Fig. 8) and NDBC buoy observations (Figs. S3 and S4), we also demonstrate the difficulties in retrieving peak wave length and wave direction under mixed sea states where wind sea and swells from different directions coexist. This challenge primarily stems from the distortion of the along-track wavenumber spectrum of ICESat-2 owing to its 1D along-track sampling, which may smear the dominant, high-frequency wind sea peak out and subsequently invalidate the geometric correction (Eq. 15) under mixed sea states (Fig. 8f). Nonetheless, it is found that the accuracy of the ICESat-2 wave height is practically not affected by the complexity of sea states. The accuracy of peak wave length and direction retrieved by ICESat-2 under mixing sea states might be augmented if the wave parameters (particularly bulk parameters for different wind sea and swell spectral partitions; Hanson et al. 2009) produced by spectral wave models (e.g., Liu et al. 2019, 2021) are used as supplementary input. Modern deep learning and machine learning tools might also useful to this end.

One noted limitation of the present paper is only in-situ wave measurements from NDBC and CDIP wave buoys are used as "ground truth", all of which are located in North Pacific and Atlantic. As one reviewer suggested, wave observations from other satellite platforms,

including wave height from simultaneously operating altimeters (e.g., Ribal and Young 2019), dominant wave length and direction from CFOSAT (Hauser et al. 2021) and SAR (Hasselmann et al. 2013), represent valuable complementary data for further validating the ICESat-2 wave records in global oceans. A thorough investigation of the cross-validation among different satellite platforms based on their crossovers is left for future research.

In conclusion, this study thoroughly evaluates and validates the capability of ICESat-2 of observing ocean surface waves in both deep and coastal waters and clearly demonstrates its limitation in mixed/multimodal sea states, particularly for observing the peak wave length and direction. The wave measurements from ICESat-2, especially significant wave height, represent important data for coastal and ocean engineering, for wave model development and validation, and for other wave-related applications.

Funding

Q.L. acknowledges the support from the Shandong Provincial Natural Science Fund for Excellent Young Scientists Fund Program (Overseas) (2023HWYQ-056), the National Natural Science Foundation of China (42106012), the Taishan Scholars Program (tsqnz20221111) and the Fundamental Research Funds for the Central Universities (202441007). A.A. acknowledges funding from EPSRC, United Kingdom (EP/Y02012X/1).

Data Availability Statement.

The ICESat-2 data are available through the National Snow Ice Data Center (NSIDC). The ATL03 geolocated photon data are found online (https://nsidc.org/data/atl03/versions/6). The NDBC buoy data used in this research are from the USACE QCC Measurement Archive, which can be downloaded from the USACE Coastal and Hydraulic Laboratory (CHL) Data server (https://chldata.erdc.dren.mil/). The CDIP buoy data are accessible on the THREDDS data server (https://thredds.cdip.ucsd.edu/thredds/catalog/cdip/archive/catalog.html). The WW3-ST6 global wave hindcast is archived at the Mediaflux platform, a data storage and management service kindly supported by the Research Computing Services of the University of Melbourne. Data access will be provided from Q. Liu (liuqingxiang@ouc.edu.cn) and A. Babanin (a.babanin@unimelb.edu.au).

677 REFERENCES

678 Aouf, L., Hauser, D., Chapron, B., Toffoli, A., Tourain, C., & Peureux, C. (2021) New
679 Directional Wave Satellite Observations: Towards Improved Wave Forecasts and Climate
680 Description in Southern Ocean. *Geophys. Res. Lett.* **48**:e2020GL091187.
681 https://doi.org/10.1029/2020GL091187

682 Ardhuin, F., Stopa, J. E., Chapron, B., Collard, F., Husson, R., Jensen, R. E., et al. (2019)
683 Observing Sea States. *Front. Mar. Sci.* **6**. https://doi.org/10.3389/fmars.2019.00124

684 Banner, M. L. (1990) Equilibrium Spectra of Wind Waves. *J. Phys. Oceanogr.* **20**:966-984.
685 https://doi.org/10.1175/1520-0485(1990)020<0966:ESOWW>2.0.CO;2

686 Booij, N., Ris, R. C., & Holthuijsen, L. H. (1999) A third-generation wave model for coastal
687 regions: 1. Model description and validation. *J. Geophys. Res.: Oceans* **104**:7649-7666.
688 https://doi.org/10.1029/98JC02622

689 Bowers, J. A., Morton, I. D., & Mould, G. I. (2000) Directional statistics of the wind and waves.
690 *Appl. Ocean Res.* **22**:13-30. https://doi.org/10.1016/S0141-1187(99)00025-5

691 Brodtkorb, P.A., Johannesson, P., Lindgren, G., Rychlik, I., Rydén, J. and Sö, E. (2000).
692 "WAFO - a Matlab toolbox for analysis of random waves and loads", *Proc. 10th Int.*
693 *Offshore and Polar Eng. Conf.*, Seattle, USA, Vol III, pp. 343-350.

694 Brouwer, J., Fraser, A. D., Murphy, D. J., Wongpan, P., Alberello, A., Kohout, A., et al. (2022)
695 Altimetric observation of wave attenuation through the Antarctic marginal ice zone using
696 ICESat-2. *The Cryosphere* **16**:2325-2353. https://doi.org/10.5194/tc-16-2325-2022

697 Brunt, K. M., Smith, B. E., Sutterley, T. C., Kurtz, N. T., & Neumann, T. A. (2021)
698 Comparisons of Satellite and Airborne Altimetry With Ground-Based Data From the
699 Interior of the Antarctic Ice Sheet. *Geophys. Res. Lett.* **48**:e2020GL090572.
700 https://doi.org/10.1029/2020GL090572

701 Chawla, A., Spindler, D. M., & Tolman, H. L. (2013) Validation of a thirty year wave hindcast
702 using the Climate Forecast System Reanalysis winds. *Ocean Modell.* **70**:189-206.
703 https://doi.org/10.1016/j.ocemod.2012.07.005

704 Chelton, D. B., Ries, J. C., Haines, B. J., Fu, L.-L., & Callahan, P. S. (2001) Chapter 1 Satellite
705 Altimetry. In: L.-L. Fu, & A. Cazenave (ed) *International Geophysics*. Academic Press, pp
706 1-ii. https://doi.org/10.1016/S0074-6142(01)80146-7

Collard, F., Marié, L., Nouguier, F., Kleinherenbrink, M., Ehlers, F., & Ardhuin, F. (2022) Wind-Wave Attenuation in Arctic Sea Ice: A Discussion of Remote Sensing Capabilities. *J. Geophys. Res.: Oceans* **127**:e2022JC018654. https://doi.org/10.1029/2022JC018654

Dietrich, J. T., Magruder, L. A., & Holwill, M. (2023) Monitoring Coastal Waves with ICESat-2. *J. Mar. Sci. Eng.* **11**:2082. https://doi.org/10.3390/jmse11112082

Dodet, G., Leckler, F., Sous, D., Ardhuin, F., Filipot, J. F., & Suanez, S. (2018) Wave Runup Over Steep Rocky Cliffs. *J. Geophys. Res.: Oceans* **123**:7185-7205. https://doi.org/10.1029/2018JC013967

Donelan, M. A., Hamilton, J., Hui, W. H., & Stewart, R. W. (1985) Directional spectra of wind-generated ocean waves. *Philosophical Transactions of the Royal Society of London. Series A, Mathematical and Physical Sciences* **315**:509-562. http://doi.org/10.1098/rsta.1985.0054

Fenton, J. D. (1988) The numerical solution of steady water wave problems. *Comput. Geosci.* **14**:357-368. https://doi.org/10.1016/0098-3004(88)90066-0

Gregory, J. M., Griffies, S. M., Hughes, C. W., Lowe, J. A., Church, J. A., Fukimori, I., et al. (2019) Concepts and Terminology for Sea Level: Mean, Variability and Change, Both Local and Global. *Surv. Geophys.* **40**:1251-1289. https://doi.org/10.1007/s10712-019-09525-z

Hall, C., & Jensen, R. E. (2022) USACE Coastal and Hydraulics Laboratory Quality Controlled, Consistent Measurement Archive. *Sci. Data* **9**:248. https://doi.org/10.1038/s41597-022-01344-z

Hanson, J. L., & Phillips, O. M. (2001) Automated Analysis of Ocean Surface Directional Wave Spectra. *J. Atmos. Oceanic Technol.* **18**:277-293. https://doi.org/10.1175/1520-0426(2001)018<0277:AAOOSD>2.0.CO;2

Hanson, J. L., Tracy, B. A., Tolman, H. L., & Scott, R. D. (2009) Pacific Hindcast Performance of Three Numerical Wave Models. *J. Atmos. Oceanic Technol.* **26**:1614-1633. https://doi.org/10.1175/2009JTECHO650.1

Hasselmann, K., Chapron, B., Aouf, L., Ardhuin, F., Collard, F., Engen, G., et al. (2013). The ERS SAR wave mode: A breakthrough in global ocean wave observations. In Y. Desnos

(Ed.), ERS Missions: 20 Years of Observing the Earth (pp. 167-197). Noordwijk: ESA/ESTEC.

Hauser, D., Tourain, C., Hermozo, L., Alraddawi, D., Aouf, L., Chapron, B., et al. (2021) New Observations From the SWIM Radar On-Board CFOSAT: Instrument Validation and Ocean Wave Measurement Assessment. *IEEE Trans. Geosci. Remote Sens.* **59**:5-26. https://doi.org/10.1109/TGRS.2020.2994372

Hell, M. C., & Horvat, C. (2024) A method for constructing directional surface wave spectra from ICESat-2 altimetry. *The Cryosphere* **18**:341-361. https://doi.org/10.5194/tc-18-341-2024

Hersbach, H., Bell, B., Berrisford, P., Hirahara, S., Horányi, A., Muñoz Sabater, J., et al. (2020) The ERA5 global reanalysis. *Q. J. R. Meteorolog. Soc.* **146**:1999-2049. https://doi.org/10.1002/qj.3803

Hithin, N. K., Remya, P. G., Nair, T. M. B., Harikumar, R., Kumar, R., & Nayak, S. (2015) Validation and Intercomparison of SARAL/AltiKa and PISTACH-Derived Coastal Wave Heights Using In-Situ Measurements. *IEEE J. Sel. Top. Appl. Earth Obs. Remote Sens.* **8**:4120-4129. https://doi.org/10.1109/JSTARS.2015.2418251

Horvat, C., Blanchard-Wrigglesworth, E., & Petty, A. (2020) Observing Waves in Sea Ice With ICESat-2. *Geophys. Res. Lett.* **47**:e2020GL087629. https://doi.org/10.1029/2020GL087629

Kessler, W. S., & McCreary, J. P. (1993) The Annual Wind-driven Rossby Wave in the Subthermocline Equatorial Pacific. *J. Phys. Oceanogr.* **23**:1192-1207. https://doi.org/10.1175/1520-0485(1993)023<1192:TAWDRW>2.0.CO;2

Klotz, B. W., Neuenschwander, A., & Magruder, L. A. (2020) High-Resolution Ocean Wave and Wind Characteristics Determined by the ICESat-2 Land Surface Algorithm. *Geophys. Res. Lett.* **47**:e2019GL085907. https://doi.org/10.1029/2019GL085907

Liu, Q., Babanin, A. V., Guan, C., Zieger, S., Sun, J., & Jia, Y. (2016) Calibration and Validation of HY-2 Altimeter Wave Height. *J. Atmos. Oceanic Technol.* **33**:919-936. https://doi.org/10.1175/JTECH-D-15-0219.1

Liu, Q., Babanin, A. V., Rogers, W. E., Zieger, S., Young, I. R., Bidlot, J.-R., et al. (2021) Global Wave Hindcasts Using the Observation-Based Source Terms: Description and

766 Validation. *J. Adv. Model. Earth Syst.* **13**:e2021MS002493.
767 https://doi.org/10.1029/2021MS002493

768 Liu, Q., Rogers, W. E., Babanin, A. V., Young, I. R., Romero, L., Zieger, S., et al. (2019)
769 Observation-Based Source Terms in the Third-Generation Wave Model WAVEWATCH
770 III: Updates and Verification. *J. Phys. Oceanogr.* **49**:489-517. https://doi.org/10.1175/JPO-
771 D-18-0137.1

772 Liu, Q., Young, I. R., Zieger, S., Ribal, A., Long, S.-M., Dong, X., et al. (2023) On global wave
773 height climatology and trends from multiplatform altimeter measurements and wave
774 hindcast. *Ocean Modell.* **186**:102264. https://doi.org/10.1016/j.ocemod.2023.102264

775 Ma, Y., Xu, N., Liu, Z., Yang, B., Yang, F., Wang, X. H., et al. (2020) Satellite-derived
776 bathymetry using the ICESat-2 lidar and Sentinel-2 imagery datasets. *Remote Sens.*
777 *Environ.* **250**:112047. https://doi.org/10.1016/j.rse.2020.112047

778 Magruder, L., Brunt, K., Neumann, T., Klotz, B., & Alonzo, M. (2021) Passive Ground-Based
779 Optical Techniques for Monitoring the On-Orbit ICESat-2 Altimeter Geolocation and
780 Footprint Diameter. *Earth Space Sci.* **8**:e2020EA001414.
781 https://doi.org/10.1029/2020EA001414

782 Markus, T., Neumann, T., Martino, A., Abdalati, W., Brunt, K., Csatho, B., et al. (2017) The
783 Ice, Cloud, and land Elevation Satellite-2 (ICESat-2): Science requirements, concept, and
784 implementation. *Remote Sens. Environ.* **190**:260-273.
785 https://doi.org/10.1016/j.rse.2016.12.029

786 Monaldo, F. (1988) Expected differences between buoy and radar altimeter estimates of wind
787 speed and significant wave height and their implications on buoy-altimeter comparisons. *J.*
788 *Geophys. Res.: Oceans* **93**:2285-2302. https://doi.org/10.1029/JC093iC03p02285

789 Morison, J., Dickinson, S., Hancock, D., Robbins, J., & Roberts, L. (2022) ICESat-2 ATL12
790 Ocean Surface Height and ATL19 Gridded Dynamic Ocean Topography. *OCEANS 2022,*
791 *Hampton Roads*, Hampton Roads, VA, USA, 2022, pp. 1-6.
792 http://doi.org/10.1109/OCEANS47191.2022.9977076

793 Neumann, T. A., Brenner, A., Hancock, D., Robbins, J., Gibbons, A., Lee, J., et al. (2023)
794 ATLAS/ICESat-2 L2A Global Geolocated Photon Data. (ATL03, Version 6). [Data Set].
795 Boulder, Colorado USA. NASA National Snow and Ice Data Center Distributed Active
796 Archive Center, accessed 11 December 2024. https://doi.org/10.5067/ATLAS/ATL03.006

797 Neumann, T. A., Martino, A. J., Markus, T., Bae, S., Bock, M. R., Brenner, A. C., et al. (2019)
798 The Ice, Cloud, and Land Elevation Satellite – 2 mission: A global geolocated photon
799 product derived from the Advanced Topographic Laser Altimeter System. *Remote Sens.*
800 *Environ.* **233**:111325. https://doi.org/10.1016/j.rse.2019.111325

801 Neumann, T., Magruder, L., & Kurtz, N. (2022) ICESat-2 Mission: Contributions of a
802 spaceborne lidar to ocean science. *OCEANS 2022, Hampton Roads*, Hampton Roads, VA,
803 USA, 2022, pp. 1-5. https://doi.org/10.1109/OCEANS47191.2022.9977260

804 Nilsson, B., Andersen, O. B., Ranndal, H., & Rasmussen, M. L. (2022) Consolidating ICESat-
805 2 Ocean Wave Characteristics with CryoSat-2 during the CRYO2ICE Campaign. *Remote*
806 *Sens.* **14**:1300. https://doi.org/10.3390/rs14061300

807 Passaro, M., Cipollini, P., Vignudelli, S., Quartly, G. D., & Snaith, H. M. (2014) ALES: A
808 multi-mission adaptive subwaveform retracker for coastal and open ocean altimetry.
809 *Remote Sens. Environ.* **145**:173-189. https://doi.org/10.1016/j.rse.2014.02.008

810 Pavlis, N. K., Holmes, S. A., Kenyon, S. C., & Factor, J. K. (2012) The development and
811 evaluation of the Earth Gravitational Model 2008 (EGM2008). *J. Geophys. Res.: Solid*
812 *Earth* **117**:B04406. https://doi.org/10.1029/2011JB008916

813 Piscopo, V., Rossi, G. B., Crenna, F., Gaglione, S., Scamardella, A., Uttieri, M., et al. (2022)
814 Measurement of Sea Waves. In: P. Daponte, G. B. Rossi, & V. Piscopo (ed) *Measurement*
815 *for the Sea: Supporting the Marine Environment and the Blue Economy*. Springer
816 International Publishing, Cham, pp 157-179. https://doi.org/10.1007/978-3-030-82024-4_7

817 Ribal, A., & Young, I. R. (2019) 33 years of globally calibrated wave height and wind speed
818 data based on altimeter observations. *Sci. Data* **6**:77. https://doi.org/10.1038/s41597-019-
819 0083-9

820 Rogers, W.E., Dykes, J.D., and Wittmann, P.A. (2014) US Navy global and regional wave
821 modeling. *Oceanography* **27**:56–67. https://doi.org/10.5670/oceanog.2014.68

822 Shao, W., Li, X., Hwang, P., Zhang, B., & Yang, X. (2017), Bridging the gap between cyclone
823 wind and wave by C-band SAR measurements, *J. Geophys. Res. Oceans*, **122:** 6714–6724.

824 The WAMDI Group (1988) The WAM model - A third generation ocean wave prediction
825 model. *J. Phys. Oceanogr.* **18**:1775–1810. https://doi.org/10.1175/1520-
826 0485(1988)018<1775:TWMTGO>2.0.CO;2

The WAVEWATCH III ® Development Group (WW3DG) (2019) User manual and system documentation of WAVEWATCH III® version 6.07. Tech. Note 333. NOAA/NWS/NCEP/MMAB, College Park, MD, USA, 465 pp. + Appendices.

Tolman, H. L., Balasubramaniyan, B., Burroughs, L. D., Chalikov, D. V., Chao, Y. Y., Chen, H. S., et al. (2002) Development and Implementation of Wind-Generated Ocean Surface Wave Modelsat NCEP. *Weather Forecasting* **17**:311-333. https://doi.org/10.1175/1520-0434(2002)017<0311:DAIOWG>2.0.CO;2

Torsethaugen K, Haver S (2004) Simplified double peak spectral model for ocean waves. In: *Proceedings of the 14th international offshore and polar engineering conference*, Toulon.

Voermans, J. J., Fraser, A. D., Brouwer, J., Meylan, M. H., Liu, Q., & Babanin, A. V. (2024) Finely-resolved along-track wave attenuation estimates in the Antarctic marginal ice zone from ICESat-2. *EGUsphere* **2024**:1-20. https://doi.org/10.5194/egusphere-2024-2104

Welch, P. (1967) The use of fast Fourier transform for the estimation of power spectra: A method based on time averaging over short, modified periodograms. *IEEE Trans. Audio Electroacoust.* **15**:70-73. https://doi.org/10.1109/TAU.1967.1161901

Yang, J., Ma, Y., Zheng, H., Xu, N., Zhu, K., Wang, X. H., et al. (2022) Derived Depths in Opaque Waters Using ICESat-2 Photon-Counting Lidar. *Geophys. Res. Lett.* **49**:e2022GL100509. https://doi.org/10.1029/2022GL100509

Young, I. R. (1999) Chapter 9 - Ocean Wave Measurement. In: I. R. Young (ed) *Elsevier Ocean Engineering Series*. Elsevier, pp 227-254. https://doi.org/10.1016/S1571-9952(99)80011-7

Yu, Y., Sandwell, D. T., Gille, S. T., & Bôas, A. B. V. (2021) Assessment of ICESat-2 for the recovery of ocean topography. *Geophys. J. Int.* **226**:456-467. https://doi.org/10.1093/gji/ggab084

Zieger, S., Vinoth, J., & Young, I. R. (2009) Joint Calibration of Multiplatform Altimeter Measurements of Wind Speed and Wave Height over the Past 20 Years. *J. Atmos. Oceanic Technol.* **26**:2549-2564. https://doi.org/10.1175/2009JTECHA1303.1